ISSN 0021-3640, JETP Letters, 2016, Vol. 104, No. 5, pp. 309–314. © Pleiades Publishing, Inc., 2016.
Original Russian Text © A.M. Tikhonov, 2016, published in Pis'ma v Zhurnal Eksperimental'noi i Teoreticheskoi Fiziki, 2016, Vol. 104, No. 5, pp. 318–324.

CONDENSED MATTER

Diffuse X-Ray Scattering near a Two-Dimensional Solid–Liquid Phase Transition at the *n*-Hexane–Water Interface

A. M. Tikhonov*

Kapitza Institute for Physical Problems, Russian Academy of Sciences, Moscow, 119334 Russia
**e-mail: tikhonov@kapitza.ras.ru*

Received July 5, 2016; in final form, July 19, 2016

According to experimental data on X-ray scattering and reflectometry with synchrotron radiation, a two-dimensional crystallization phase transition in a monolayer of melissic acid at the *n*-hexane–water interface with a decrease in the temperature occurs after a wetting transition.

DOI: 10.1134/S0021364016170124

The observation of a two-dimensional solid–liquid phase transition at the oil–water interface was reported in [1–3]. In this work, the temperature dependence of the intensity of diffuse (nonspecular) scattering of 15-keV photons at the *n*-hexane–water interface, where such a transition occurs in the adsorbed layer of melissic acid (C_{30}-acid) [3], is studied. It is shown below that the diffuse scattering intensity in the low-temperature crystal phase at the interface is one or two orders of magnitude higher than that in the high-temperature phase, which indicates the existence of an extended transverse structure with a thickness of ~ 200 Å in the former phase. The analysis of experimental data within the theory of capillary waves indicates that the two-dimensional crystallization transition at the interface with a decrease in the temperature occurs after the wetting transition.

Samples of macroscopically flat *n*-hexane–water interface were prepared and studied by the method presented in [4, 5] in a stainless steel cell with dimensions of the interface of 75×150 mm whose temperature was controlled by means of a two-stage thermostat. Systems with the volume concentration of C_{30}-acid in *n*-hexane $c \approx 0.2$ mmol/kg ($\approx 2\times10^{-5}$) and the amount of material sufficient for covering of the interface with $\sim10^2$ monolayers of acid were studied. Saturated hydrocarbon C_6H_{14} with the boiling temperature $T_b \approx 342$ K and the density at 298 K ≈ 0.65 g/cm^3 was preliminarily purified by multiple filtration in a chromatographic column. A solution of sulfuric acid (pH = 2) in deionized water (Barnstead, NanoPureUV) was used as the lower bulk phase, where $C_{30}H_{60}O_2$ is hardly dissolved. The diffuse scattering intensity was measured for a sample that was aged for no less than 12 h after a change in the temperature of the cell. In order to prevent the formation of gas bubbles at the interface, the sample was "annealed": the liquids in the cell were heated to $T \cong T_b$ and were then cooled below T_c.

The reflectometry data obtained with synchrotron radiation previously reported for this system show that molecules of C_{30}-acid are adsorbed at the *n*-hexane–water interface in form of the Gibbs monolayer with the thermodynamic parameters (p,T,c) [3]. A sharp phase transition from a crystal state with the area per molecule $A = 17 \pm 1$ Å^2 to a liquid state with the area per molecule $A = 23 \pm 1$ Å^2 occurs in the monolayer at a pressure of $p = 1$ atm and a temperature of $T_c \approx 293.5$ K. The density of the low-temperature solid phase of the Gibbs monolayer corresponds to the packing in the crystal phase of Langmuir monolayer of C_{30}-acid on the surface of water and is close to the volume density of the corresponding crystal [6, 7]. The density of the high-temperature phase is close to the density of a high-molecular-weight hydrocarbon liquid and corresponds to, e.g., the density of the liquid phase of the Gibbs monolayer of melissyl alcohol at the *n*-hexane–water interface [7, 8].

With an increase in the temperature in a close vicinity of T_c ($\Delta T < 0.2$ K), a significant fraction of C_{30}-acid molecules adsorbed in a solid monolayer leave the interface and are dissolved in the bulk of *n*-hexane: the density of the monolayer decreases by ≈30% and the thickness of the monolayer simultaneously decreases by ≈15%. For both phases, a qualitative two-layer model satisfactorily describes reflectometry data and is in agreement with the structure of a linear chain molecule of melissic acid $C_{30}H_{60}O_2$ with a length of ≈41 Å. The formation of the first layer involves polar head parts COOH, whereas the second

layer is formed by hydrophobic hydrocarbon tails $C_{29}H_{59}$.

The scattering intensity I at the n-hexane–water interface was measured by a universal spectrometer for studying the surface of the liquid at the X19C station of the NSLS synchrotron [9]. In experiments, a focused monochromatic beam with the wavelength $\lambda = 0.825 \pm 0.002$ Å and an intensity of ~10^{10} photons/s was used. Owing to a large depth of penetration of radiation into the hydrocarbon solvent (≈19 mm) and a quite high brightness of the source of synchrotron radiation (bending magnet), scattering data can provide information on the microstructure of the surface layer supplementing previous reflectometry data.

In grazing geometry, the kinematics of scattering on the macroscopically flat interface oriented by the gravitational force is conveniently described in the coordinate system whose origin O is at the center of the illuminated region, the xy plane coincides with the interface between the monolayer and water, the Ox axis is perpendicular to the beam direction, and the Oz axis is normal to the surface and is opposite to the gravitational force (see Fig. 1). Let $\mathbf{k}_{in}$ and $\mathbf{k}_{sc}$ be the wave vectors of the incident and scattered beams with the amplitude $k_0 = 2\pi/\lambda$ in the direction of the observation point, respectively. The grazing angle $\alpha \ll 1$ and scattering angle $\beta \ll 1$ lie in the yz plane, and $\varphi \approx 0$ is the angle between the incident beam and scattering direction in the xy plane. In the case of specular reflection ($\alpha = \beta$, $\varphi = 0$), the scattering vector $\mathbf{q} = \mathbf{k}_{in} - \mathbf{k}_{sc}$ is directed along the Oz axis and has the length $q_z = k_0(\sin\alpha + \sin\beta) \approx 2k_0\alpha$. At $\alpha \neq \beta$, the scattering vector $\mathbf{q}$ has the components $q_x = k_0\cos\beta\sin\varphi \approx k_0\varphi$ and $q_y = k_0(\cos\beta\cos\varphi - \cos\alpha) \approx k_0(\alpha^2 - \beta^2)/2$ in the plane of interface.

When measuring the scattering intensity $I(\beta)$, the vertical size of the incident beam with the angular divergence $\Delta\alpha = d/l \approx 10^{-4}$ rad near the surface of the sample was ≈ 0.05 mm and was controlled by a pair of collimating slits with the vertical gap $d = 0.05$ mm spaced by the distance $l \approx 60$ cm. The distance from the input slit in front of the sample to the detector was $L_1 \approx 90$ cm. The gap in all slits in the horizontal plane was $D \approx 10$ mm, which was much larger than the horizontal size of the incident beam ~2 mm. The intensity $I(\beta)$ was measured by a point detector with the angular resolution in the horizontal plane $\Delta\varphi = D/L_1 \approx 10^{-2}$ rad and with the angular resolution in the plane of incidence $\Delta\beta = 2H_d/L_2 \approx 3 \times 10^{-4}$ rad, where $2H_d = 0.2$ mm is the gap in the slit in front of the detector and $L_2 \approx 70$ cm is the distance from the center of the sample.

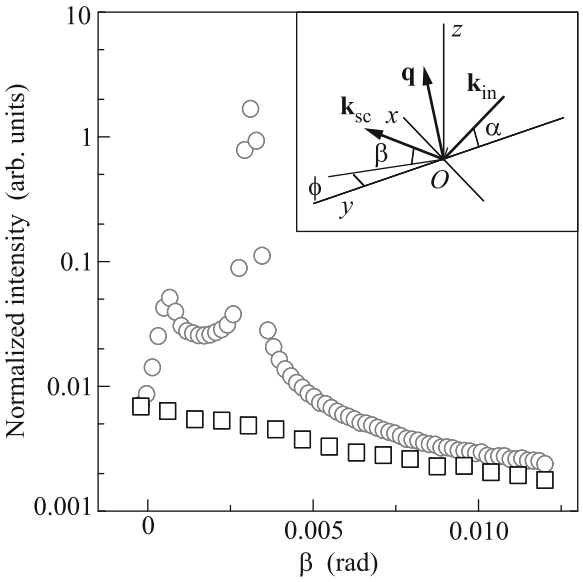

Fig. 1. Angular dependences of the scattering intensity at the grazing angle $\alpha \approx 3.3 \times 10^{-3}$ rad (≈0.19°) and $T = 293.2$ K: (circles) the total scattering intensity $I(\beta)/I_0$ and (squares) background from the scattering of the incident beam in the bulk of n-hexane I_b/I_0. The inset shows the kinematics of scattering in the coordinate system where the xy plane coincides with the boundary between the monolayer and water, the Ox axis is perpendicular to the direction of the beam, and the Oz axis is directed along the normal to the surface against the gravitational force.

Below, I_0 is a quantity proportional to the intensity of the incident beam, which was controlled in the experiment immediately before the entrance of the beam to the cell. Circles in Fig. 1 are the data on the normalized scattering intensity $I(\beta)/I_0$ measured at the grazing angle $\alpha \approx 3.3 \times 10^{-3}$ rad (≈0.19°) and $T = 293.2$ K. Each point is obtained by summation of photons specularly reflected and diffusely scattered by the surface in the illuminated region with an area of $A_0 \approx 30$ mm^2 at the center of the interface of the sample in the direction β and I_b photons scattered in the bulk of n-hexane on the path to the interface. For the independent determination of the contribution I_b in $I(\beta)$, the experimental sample cell was displaced down along the Oz axis by ~0.2 mm so that the beam propagated slightly above the interface. In this case, the detected background increased to $\approx 2I_b$, because the length of the path of the photon beam in the hydrocarbon solvent increased by a factor of about 2. The background I_b/I_0 thus measured is shown by squares in Fig. 1.

Figures 2 and 3 show the data on the normalized surface scattering intensity $I_n(\beta) \equiv (I(\beta) - I_b)/I_0$

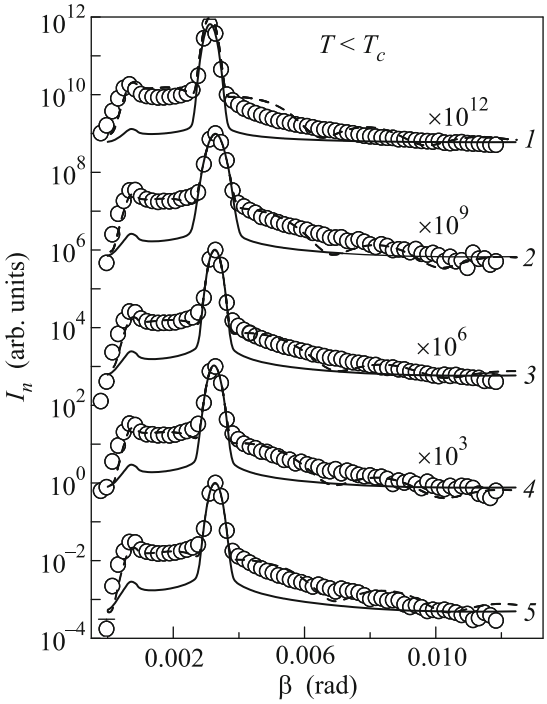

Fig. 2. Angular dependences of the surface scattering intensity I_n at the grazing angle $\alpha \approx 3.3 \times 10^{-3}$ rad for the *n*-hexane–water interface at various temperatures $T < T_c$: $T =$ (*1*) 294, (*2*) 290, (*3*) 289, (*4*) 287, and (*5*) 285 K. The solid lines correspond to the monolayer model given by Eq. (13), whereas the dashed lines correspond to the extended-layer model specified by Eq. (14).

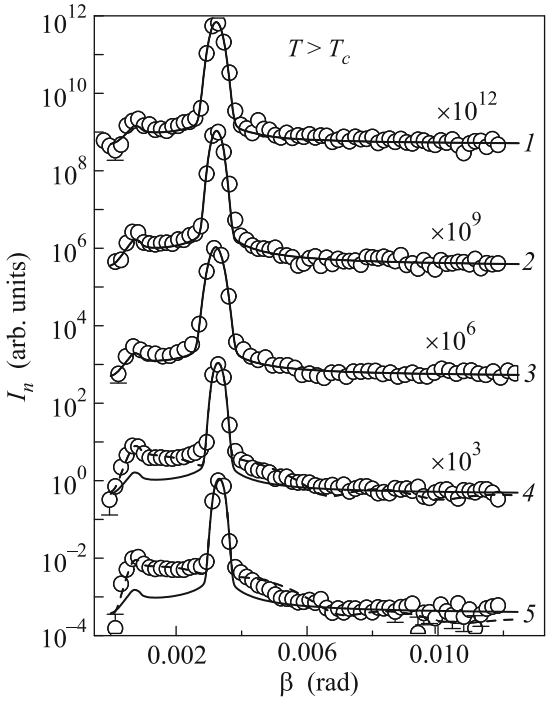

Fig. 3. Angular dependences of the surface scattering intensity I_n at the grazing angle $\alpha \approx 3.3 \times 10^{-3}$ rad for the *n*-hexane–water interface at various temperatures $T > T_c$: $T =$ (*1*) 335, (*2*) 323, (*3*) 318, (*4*) 308, and (*5*) 298 K. The solid lines correspond to the monolayer model given by Eq. (13), whereas the dashed lines correspond to the extended-layer model specified by Eq. (14).

(normalization condition $I_n(\alpha) \equiv 1$) obtained in the temperature range of 285 to 335 K. The most intense peak on curves corresponds to the specular reflection $\beta = \alpha$, whereas the peak against the diffuse background at $\beta \to 0$ corresponds to the angle of total external reflection $\alpha_c \approx 10^{-3}$ rad ($\approx 0.05°$) [10]. Scattering occurs in the range of the characteristic in-plane lengths $2\pi/q_y \sim 10^{-5}$–10^{-6} m. The long-wavelength limit is specified by the vertical resolution of the detector $\Delta\beta$, where the short-wavelength limit is specified by the maximum value $\beta \sim 1.2 \times 10^{-2}$ rad ($\approx 0.7°$) at which the surface and bulk components in the scattering intensity can still be separated from each other.

In the distorted wave Born approximation (DWBA), the surface scattering intensity I_n of the monochromatic photon beam I_0 is the sum of diffuse scattering I_{diff} and specular reflection I_{spec} [11, 12]

$$I_n = I_{\text{diff}} + I_{\text{spec}}. \qquad (1)$$

Below, we examine only nonspecular scattering of photons by thermal fluctuations of the surface of the liquid (capillary waves), which are described by the correlation function [13–17]

$$\langle z(0)z(r)\rangle = \frac{k_B T}{2\pi\gamma} K_0\left[\left(\frac{g\Delta\rho_m}{\gamma}(r^2 + r_0^2)\right)^{1/2}\right], \qquad (2)$$

where $r^2 = x^2 + y^2$ is the square of the distance between two points on the surface, g is the gravitational acceleration, γ is the surface tension coefficient, k_B is the Boltzmann constant, $\Delta\rho_m \approx 0.34$ g/cm^3 is the difference between the densities of water and *n*-hexane, $K_0(t)$ is the modified Bessel function of the second kind, and r_0 is determined by the square of the rms width of the interface $\sigma_{cw}^2 = (k_B T)/(2\pi\gamma) K_0(r_0\sqrt{g\Delta\rho_m/\gamma})$.

The averaging of I_{diff} over grazing angles α gives

$$I_{\text{diff}} = \frac{1}{\Delta\alpha}\int\limits_{\alpha-\Delta\alpha/2}^{\alpha+\Delta\alpha/2} \frac{1}{\sin\alpha}\int\limits_{\Delta\Omega}\left(\frac{d\sigma}{d\Omega}\right)_{\text{diff}} d\Omega d\alpha, \qquad (3)$$

where $d\Omega = \sin(\pi/2 - \beta) d\beta d\varphi \approx d\beta d\varphi$ and $\Delta\Omega$ is the solid angle of photon collection by the detector. The

differential cross section for diffuse scattering is given by the expression [11]

$$\left(\frac{d\sigma}{d\Omega}\right)_{\text{diff}} = \frac{q_c^4}{(16\pi)^2}|T(\alpha)|^2|T(\beta)|^2|\Phi(\sqrt{q_z q_z^t})|^2 S(\mathbf{q}^t), \quad (4)$$

where the z component of the scattering vector in the lower phase has the form

$$q_z^t = \frac{2\pi}{\lambda}\left[(\alpha^2 - \alpha_c^2)^{1/2} + (\beta^2 - \alpha_c^2)^{1/2}\right]. \quad (5)$$

The angle of total external reflection α_c ($q_c = 2k_0 \sin\alpha_c$) is related to the difference $\Delta\rho \approx 0.11\, e^-/\text{Å}^3$ between the volume electron densities of n-hexane ($\rho_h \approx 0.22\ e^-/\text{Å}^3$) and water ($\rho_w \approx 0.33\, e^-/\text{Å}^3$): $\alpha_c = \lambda\sqrt{r_e\Delta\rho/\pi} \approx 10^{-3}$ rad, where $r_e = 2.814\times10^{-5}$ Å is the classical radius of the electron. In Eq. (4), the Fresnel transmission coefficient $T(\theta)$ for the amplitude of the wave with the polarization of synchrotron radiation on the plane of the interface is given by the formula

$$T(\theta) = \frac{2\theta}{\theta + (\theta^2 - \alpha_c^2)^{1/2}}, \quad (6)$$

and the structure factor of the interface,

$$\Phi(q) = \frac{1}{\Delta\rho}\int_{-\infty}^{+\infty}\left\langle\frac{d\rho(z)}{dz}\right\rangle e^{iqz}dz, \quad (7)$$

is determined by the Fourier transform averaged over the illuminated area A_0 of the derivative of the electron density distribution $\rho(z)$ along the Oz axis. The last factor in Eq. (4) has the form

$$S(\mathbf{q}^t) \approx \int\int_{A_0}\langle z(0)z(r)\rangle e^{iq_x x + iq_y y}dxdy \quad (8)$$

at $q_z^2\langle z(0)z(r)\rangle \ll 1$.

The substitution of Eq. (4) into Eq. (3) and the subsequent integration over the variables φ and x simplify the two-dimensional Fourier transform $\langle z(0)z(x,y)\rangle$ to a one-dimensional Fourier transform in variable y. Further, using the relation $F_t[K_0(|t|)](\omega) = \sqrt{\pi/(2\omega^2+2)}$ for the Fourier transform, we obtain

$$I_{\text{diff}} \approx \frac{\lambda q_c^4}{512\pi^2}\frac{k_B T}{\Delta\alpha\gamma} \times \int_{\alpha-\Delta\alpha/2}^{\alpha+\Delta\alpha/2}\int_{\beta-\Delta\beta/2}^{\beta+\Delta\beta/2}\frac{|T(\alpha)|^2|T(\beta)|^2|\Phi(\sqrt{q_z q_z^t})|^2}{\alpha\sqrt{q_y^2 + g\Delta\rho_m/\gamma}}d\beta\, d\alpha. \quad (9)$$

The further integration in Eq. (9) is performed numerically.

The intensity of specular reflection in Eq. (1) is given by the expression

$$I_{\text{spec}} = f(\alpha,\beta)R(\alpha), \quad (10)$$

where the reflection coefficient

$$R(\alpha) = \left|\frac{q_z - q_z^t}{q_z + q_z^t}\right|^2\left|\Phi(\sqrt{q_z q_z^t})\right|^2 \quad (11)$$

is calculated at $\alpha \equiv \beta$ with the use of Eqs. (5) and (7).

The instrumental angular resolution function $f(\alpha,\beta)$, which includes the Gaussian distribution of the intensity of the beam in the plane of incidence, has the form [17]

$$f(\alpha,\beta) = \frac{1}{2}\left[\text{erf}\left(\frac{H + H_d}{\sqrt{2}L_1\Delta\alpha}\right) - \text{erf}\left(\frac{H - H_d}{\sqrt{2}L_1\Delta\alpha}\right)\right], \quad (12)$$

where $H = (\beta - \alpha)L_2$ and the error function $\text{erf}(t) = (2/\sqrt{\pi})\int_0^t e^{-s^2}ds$ provides better agreement with experiments than the simplest trapezoidal resolution function [14].

On one hand, according to experimental data shown in Fig. 2, the diffuse background at small β values in the solid phase reaches $\approx 5\times10^{-2}$ of the height of the specular reflection peak and hardly depends on the temperature up to T_c at which R changes stepwise. On the other hand, the data shown in Fig. 3 indicate a gradual decrease in the scattering intensity I_{diff} to $\approx 2\times10^{-3}$ in the liquid phase with an increase in the temperature from T_c to $T^* \approx 320$ K.

In [3, 5], the phases of the monolayer of melissic acid were described within a qualitative two-layer model with the structure factor (7) of the form

$$\Phi(q)_m = \frac{e^{-\sigma_R^2 q^2/2}}{\Delta\rho}\sum_{j=0}^{2}(\rho_{j+1} - \rho_j)e^{-iqz_j}, \quad (13)$$

where $z_0 = 0$, $\rho_0 = \rho_w$, and $\rho_3 = \rho_h$. For the solid phase, the electron densities are $\rho_1 \approx 1.16\rho_w$ and $\rho_2 \approx 1.02\rho_w$ and the coordinates of the interfaces between the layers are $z_1 \approx 15$ Å and $z_2 \approx 41$ Å (the length of the C_{30}-acid). In the liquid phase of the monolayer, $\rho_1 \approx 1.1\rho_w$, $\rho_2 \approx 0.77\rho_w$, $z_1 \approx 18$ Å, and $z_2 \approx 36$ Å.

The exponent σ_R in Eq. in (13) presents the contribution of capillary waves to the structure of the interface. Its square $\sigma_R^2 \approx (k_B T/2\pi\gamma)\ln(Q_{\max}/Q_{\min})$ is specified by the short-wavelength limit in the spectrum of thermal fluctuations of the interface $Q_{\max} = 2\pi/a$ ($a \approx 10$ Å is about the molecular radius) and by the angular resolution of the detector

$Q_{\min} = q_z\Delta\beta/2$ ($q_z = 0.05$ Å^{-1}) [15, 18–22]. The parameter σ_R in the experiments varies from 4 to 6 Å.

The intensities I_n calculated with $\Phi(q)_m$ are shown by solid lines in Figs. 2 and 3. The observed intensity in the solid phase at $T < T_c$ is more than an order of magnitude larger than the calculated value. At the same time, the experimental data for the liquid phase of the monolayer at $T > T^*$ are well described by Eq. (13) without the variation of the parameters of the layer. Thus, scattering at $T < T^*$ occurs on a structure more complex than the homogeneous monolayer and a transition from the solid phase of the surface to the liquid monolayer occurs at two stages with the temperatures T_c and T^*.

The simplest three-layer model that qualitatively explains scattering data shown in Figs. 2 and 3 (dashed lines) and simultaneously reflectometry data reported in [3, 5] is parameterized by the structure factor of the form (see Fig. 4a)

$$\Phi(q)_m^* + \frac{\delta\rho e^{-\sigma^2 q^2/2}}{\Delta\rho} e^{-iqz_3}. \qquad (14)$$

Here, the second term describes the third adsorbed homogeneous layer with the thickness $z_3 - z_2$ and density $\rho_h + \delta\rho$, σ is the width of the interface between this layer and bulk of *n*-hexane, and $\Phi(q)_m^*$ is specified by Eq. (13) with the change $\rho_3 \to \rho_h + \delta\rho$. At $T > T^*$, the excess surface density vanishes: $\delta\rho(z_3 - z_2) = 0$.

The joint analysis of the data for I_n and $R(q_z)$ with the use of Eq. (14) shows that all parameters of the layer at $T < T_c$ hardly depend on the temperature T. Both nonspecular scattering at small β values ($\sigma^2 q_z^2 \ll 1$) and reflectometry data are satisfactorily described at the following parameters of the third layer: $z_3 - z_2 \sim 200$ Å, $\delta\rho \approx 0.1\rho_w$–$0.25\rho_w$, and $\sigma \approx 10$–20 Å. Since the contribution to $R(q_z)$ from the second term in Eq. (14) decreases rapidly with an increase in q_z and becomes negligibly small at $q_z > 0.075$ Å^{-1}, the correction of the parameters of the solid monolayer in $\Phi(q)_m^*$ is insignificant (within the error). Finally, the existing data and the used approach cannot provide a reliable determination of the parameters of the possible internal structure of the third layer.

The electron density in the third layer $\rho_h + \delta\rho$ at $T < T_c$ corresponds to a high-molecular-weight alkane liquid [7]. The fraction of melissic acid in this layer is estimated as $f = \delta\rho/(\rho_m - \rho_h) \approx 0.8$, where $\rho_m \approx 0.9\rho_w$ is the density of the liquid monolayer of C_{30}-acid. According to Fig. 3, $\delta\rho(z_3 - z_2) \to 0$ in the intermediate region $T_c < T < T^*$ at $T \to T^*$. Unfortunately, existing data are insufficient to obtain detailed information on this asymptotic behavior.

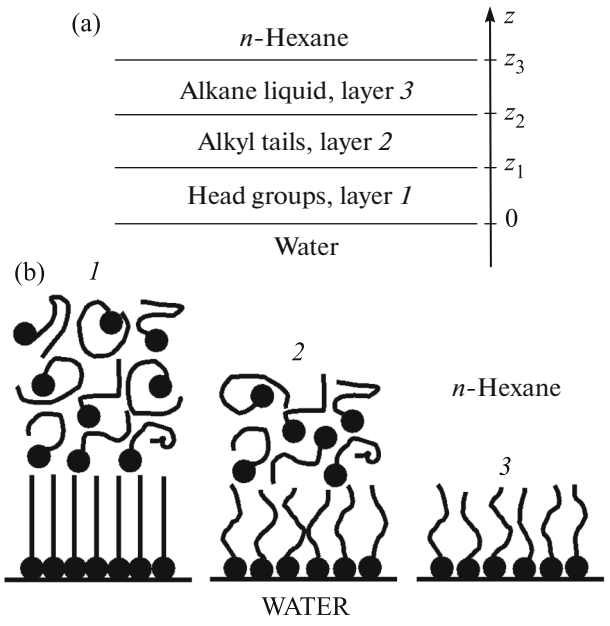

Fig. 4. (a) Three-layer model of the adsorbed layer of melissic acid $C_{30}H_{60}O_2$ at the *n*-hexane–water interface. (b) Transverse structure of the *n*-hexane–water interface: (*1*) the thick layer with a crystalline monolayer at $T < T_c$, (*2*) the layer with a liquid monolayer in the intermediate region $T_c < T < T^*$, and (*3*) the homogeneous liquid monolayer at $T > T^*$.

The formation of a multilayer structure at the alkane–water interface was previously detected in adsorbed layers of some monohydric alcohols and, more recently, in layers of mixtures of fluorocarbon alcohols [23, 24]. For example, the low-temperature phase of dodecanol adsorbed at the *n*-hexane–water interface is a high-molecular-weight alkane liquid whose density is equal to the density of the layer of melissic acid in the transitional region $T_c < T < T^*$. Nevertheless, the two-dimensional evaporation phase transition in dodecanol is fundamentally different from the melting transition in the C_{30}-acid because it is described by only a single critical temperature.

Two-dimensional phase transitions in two stages are characteristic of systems, e.g., with surface active mixtures of fluorocarbon and hydrocarbon alcohols [25]. The existence of two critical temperatures was mentioned in [2], where the crystallization of monolayers of cation surfactants CTAB and STAB was considered. However, in both cases, the authors discussed the structures of monolayers rather than extended multilayer structures.

Finally, Fig. 5 shows profiles of the electron density for surface structures (see Fig. 4b). The structure *1* at $T < T_c$ (Fig. 5) consists of a solid monolayer with a

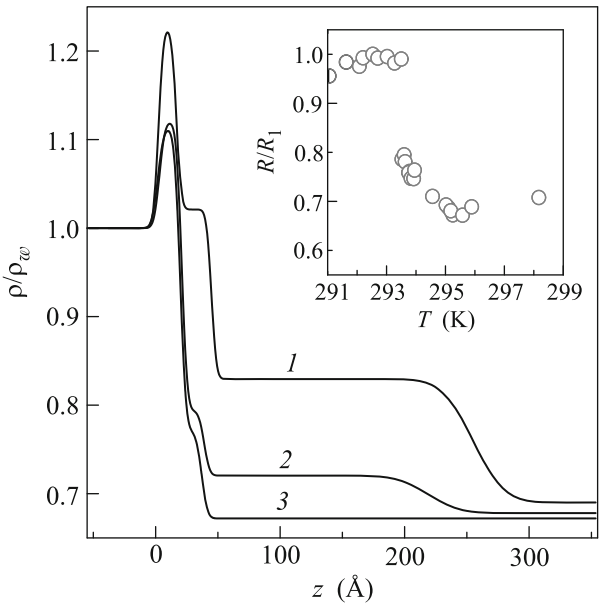

Fig. 5. Model profiles of the electron density: (*1*) the three-layer model with a solid monolayer ($T < T_c$), (*2*) the three-layer model in the intermediate region ($T_c < T < T^*$), and (*3*) the two-layer model of a liquid monolayer ($T > T^*$). The inset shows the temperature dependence of the normalized reflection coefficient R/R_1 at $q_z = 0.05$ Å^{-1}, where R_1 is the reflection coefficient at $T \approx 292.2$ K.

thickness of ≈41 Å and a layer of a high-molecular-weight alkane liquid with a thickness of ~200 Å. With an increase in the temperature, a sharp jump occurs in the reflection coefficient at $T_c \approx 293.5$ K (see the inset in Fig. 5), which indicates the melting of the monolayer of melissic acid immediately at the interface with *n*-hexane (structure *2*, Fig. 5). With a further increase in the temperature, $\delta\rho(z_3 - z_2) \to 0$, which is accompanied by a decrease in the diffuse scattering intensity. At $T > T^* \approx 320$ K, only the liquid monolayer of C_{30}-acid with a thickness of ≈36 Å remains at the interface (structure *3*, Fig. 5). Such a behavior of the system indicates that the two-dimensional crystallization phase transition in the interface occurs with a decrease in the temperature T at T_c after the wetting phase transition at T^*.

I am grateful to Profs. M.L. Schlossman and V.I. Marchenko for stimulating discussions of the experimental results. This work was perfromed using the resources of the National Synchrotron Light Source, U.S. Department of Energy (DOE) Office of Science User Facility operated for the DOE Office of Science by the Brookhaven National Laboratory under contract no. DE-AC02-98CH10886. The X19C beamline was supported by the ChemMatCARS National Synchrotron Resource, University of Chicago, University of Illinois at Chicago, and Stony Brook University.

REFERENCES

1. Q. Lei and C. D. Bain, Phys. Rev. Lett. **92**, 176103 (2004).
2. L. Tamam, D. Pontoni, Z. Sapir, Sh. Yefet, E. Sloutskin, B. M. Ocko, H. Reichert, and M. Deutsch, Proc. Natl. Acad. Sci. **108**, 5522 (2011).
3. A. M. Tikhonov, JETP Lett. **102**, 552 (2015).
4. D. M. Mitrinovic, Z. J. Zhang, S. M. Williams, Z. Q. Huang and M. L. Schlossman, J. Phys. Chem. B **103**, 1779 (1999).
5. A. M. Tikhonov, H. Patel, S. Garde, and M. L. Schlossman, J. Phys. Chem. B **110**, 19093 (2006).
6. D. Jacquemain, F. Leveiller, S. P. Weinbach, M. Lahav, L. Leiserowitz, K. Kjaer, and J. Als-Nielsen, J. Am. Chem. Soc. **113**, 7684 (1991).
7. D. M. Small, *The Physical Chemistry of Lipids* (Plenum, New York, 1986).
8. A. M. Tikhonov and M. L. Schlossman, J. Phys. Chem. B **107**, 3344 (2003).
9. M. L. Schlossman, D. Synal, Y. Guan, M. Meron, G. Shea-McCarthy, Z. Huang, A. Acero, S. M. Williams, S. A. Rice, and P. J. Viccaro, Rev. Sci. Instrum. **68**, 4372 (1997).
10. Y. Yoneda, Phys. Rev. **131**, 2010 (1963).
11. S. K. Sinha, E. B. Sirota, S. Garoff, and H. B. Stanley, Phys. Rev. B **38**, 2297 (1988).
12. V. Holy and T. Baumbach, Phys. Rev. B **49**, 10668 (1993).
13. F. P. Buff, R. A. Lovett, and F. H. Stillinger, Phys. Rev. Lett. **15**, 621 (1965).
14. A. Braslau, P. S. Pershan, G. Swislow, B. M. Ocko, and J. Als-Nielsen, Phys. Rev. A **38**, 2457 (1988).
15. D. K. Schwartz, M. L. Schlossman, E. H. Kawamoto, G. J. Kellogg, P. S. Pershan, and B. M. Ocko, Phys. Rev. A **41**, 5687 (1990).
16. B. R. McClain, D. D. Lee, B. L. Carvalho, S. G. J. Mochrie, S. H. Chen, and J. D. Litster, Phys. Rev. Lett. **72**, 246 (1994).
17. D. M. Mitrinovic, S. M. Williams, and M. L. Schlossman, Phys. Rev. E **63**, 021601 (2001).
18. J. D. Weeks, J. Chem. Phys. **67**, 3106 (1977).
19. A. Braslau, M. Deutsch, P. S. Pershan, A. H. Weiss, J. Als-Nielsen, and J. Bohr, Phys. Rev. Lett. **54**, 114 (1985).
20. M. L. Schlossman, M. Li, D. M. Mitrinovic, and A. M. Tikhonov, High Perform. Polym. **12**, 551 (2000).
21. A. M. Tikhonov, J. Chem. Phys **124**, 164704 (2006).
22. A. M. Tikhonov, J. Phys. Chem. C **111**, 930 (2007).
23. A. M. Tikhonov and M. L. Schlossman, J. Phys.: Condens. Matter **19**, 375101 (2007).
24. T. Takiue, T. Tottori, K. Tatsuta, H. Matsubara, H. Tanida, K. Nitta, T. Uruga, and M. Aratono, J. Phys. Chem. B **116**, 13739 (2012).
25. T. Takiue, T. Matsuo, N. Ikeda, K. Motomura, and M. Aratono, J. Phys. Chem. B **102**, 4906 (1998).

Translated by R. Tyapaev